Spatial Coherence Beamforming with Multi-Line Transmission to Enhance the Contrast of Coherent Structures in Ultrasound Images

Spatial Coherence Beamforming with Multi-Line Transmission to Enhance the Contrast of Coherent Structures in Ultrasound Images Degraded by Acoustic Clutter

Giulia Matrone*, *Member, IEEE*, Muyinatu A. Lediju Bell, *Senior Member, IEEE*, and Alessandro Ramalli, *Senior Member, IEEE*

***Abstract*—This work demonstrates that the combination of Multi-Line Transmission (MLT) and Short-Lag Spatial Coherence (SLSC) imaging improves the contrast of highly coherent structures within soft tissues, when compared to both traditional SLSC imaging and conventional Delay and Sum (DAS) beamforming. Experimental tests with small (i.e., 100 µm to 3 mm) targets embedded in homogeneous and heterogeneous backgrounds were conducted. DAS or SLSC images were reconstructed when implementing MLT with varying numbers of simultaneously transmitted beams. In images degraded by acoustic clutter, MLT SLSC achieved up to 34.1 dB better target contrast and up to 16 times higher frame-rates when compared to the more conventional single-line transmission SLSC images, with lateral resolution improvements as large as 38.2%. MLT SLSC thus represents a promising technique for clinical applications in which ultrasound visualization of highly coherent targets is required (e.g., breast microcalcifications, kidney stones, percutaneous biopsy needle tracking) and would otherwise be challenging due to the strong presence of acoustic clutter.**

***Index Terms*—Biopsy needle, coherence, high frame-rate, ultrasound imaging, kidney stone, microcalcification, Multi-Line Transmission, reflective target, Short-Lag Spatial Coherence, ultrasound beamforming.**

I. INTRODUCTION

ULTRASOUND imaging is nowadays regarded as an established diagnostic technique, which plays an important role in many medical applications, including both diagnostic examinations and interventional procedures, given its real-time capabilities, portability, and relatively low-cost [1]. A high-quality ultrasound image should ideally feature high spatial resolution and contrast, with minimal acoustic clutter, artifacts, and noise. However, it is known that a trade-off between resolution and contrast exists, and that many sources of artifacts may impair the final diagnostic outcome. This is particularly true when detecting small targets inside tissues, which is a highly challenging task, as it is hindered by clutter, aberrations due to tissue layers, multiple reflections and reverberations.

For example, in breast imaging applications, microcalcifications - small calcium deposits with sizes on the order of 0.1-1 mm - can be an important indicator of the presence of cancerous breast lesions [2], but they are difficult to detect with conventional ultrasound B-mode imaging. In particular, when microcalcifications are embedded in fibroglandular tissues, or more generally in a non-hypoechoic background, they can be confused with other small bright structures [3]. To make matters worse, in dense tissues, sound velocity changes cause acoustic clutter to appear within reconstructed images [4]. However, using higher frequencies (e.g. 10-15 MHz) can improve microcalcification detection with ultrasound, as in [2], where high sensitivity was achieved in BI-RADS4a patients by using a commercial scanner equipped with an advanced mode combining spatial and frequency compounding and a 13 MHz transducer.

Similarly, for the detection of kidney stones, ultrasound is commonly employed in clinical practice, especially in those patients for whom ionizing radiation should be avoided. The detection with B-mode imaging may be challenging when the dimension of such stones is particularly reduced (less than a few mm) [5]. Ulusan *et al.* [6] used a convex probe working in the 2-5 MHz range to demonstrate that ultrasound has limited capabilities when detecting small renal stones in the kidneys when compared to computed tomography (CT), and with sensitivity depending on the size of the stone. Ganesan *et al.* [7] additionally demonstrated that ultrasound has a lower sensitivity than CT when detecting smaller renal stones and that 27% of larger (i.e., >10 mm) stones can be missed.

An additional example of diagnostic examination in which the tracking of small reflective targets with ultrasound plays a key role is biopsy needle imaging, e.g. in the breast, liver or

Manuscript received December 9th, 2020. This work was supported in part by the University of Pavia through the Blue Sky Research project MULTIWAVE. *Asterisk indicates corresponding author.*

*G. Matrone is with the Department of Electrical, Computer and Biomedical Engineering, and with the Centre for Health Technologies, University of Pavia, 27100 Pavia, Italy (e-mail: giulia.matrone@unipv.it).

M. A. Lediju Bell is with the Department of Electrical and Computer Engineering, Johns Hopkins University, 21218 Baltimore, MD, USA (e-mail: mledijubell@jhu.edu).

A. Ramalli is with the Department of Information Engineering, University of Florence, 50139 Florence, Italy (e-mail: alessandro.ramalli@unifi.it).

kidneys. This example represents another case in which many challenges arise for interventional radiologists [8], [9], particularly due to the presence of significant sound speed variations, the multiple abdominal wall layers, and fatty tissue layers. These interventional radiology challenges cause severe acoustic clutter, due to multiple reflections and reverberations, which can impair the visibility of the needle tip and shaft during ultrasound-guided percutaneous biopsies [8], [10].

It has been shown that coherence-based beamforming techniques reduce clutter, artifacts, and improve contrast of images [11]–[15]. However, to the best of the authors' knowledge, a limited number of papers investigate coherence-based beamformers for the detection of small coherent targets in tissues. In [16], the performance of three algorithms - Aperture Domain Model Image Reconstruction (ADMIRE), Short-Lag Spatial Coherence (SLSC), and Mid-Lag Spatial Coherence - were compared for kidney stone detection. In [17], an algorithm based on coherence factor and on the dominance of the first eigenvalue of covariance matrices was proposed for breast microcalcification imaging. In both examples, B-mode images were reconstructed based on conventional scans, where image lines were acquired sequentially.

The present work instead focuses on Multi-Line Transmission (MLT), and for the first time it combines this high-frame-rate technique with SLSC imaging, showing that their joint use can provide an improved contrast of small reflective targets as compared to ultrasound images created with each option independently. In particular, this work newly exploits the main drawback of MLT (i.e., the generation of crosstalk artifacts, due to interferences between the multiple transmitted beams), based on the findings described in [18], demonstrating that MLT causes echo signals from tissues to suffer from a decorrelation effect. This effect increases with the number of simultaneously transmitted beams. Considering that spatial coherence describes the correlation between signals at different points in space [11], the decorrelation observed with MLT is characterized by a rapid drop of the spatial coherence function in the short-lag region.

Therefore, we hypothesize that this effect can be leveraged to enhance the appearance of highly-coherent structures (i.e., targets that generate strongly correlated echo signals, such as a biopsy needle) by combining MLT with SLSC imaging, which directly provides a representation of the distribution of backscattered echo spatial coherence. The decrease of correlation caused by MLT is expected to produce a darker appearance of tissue background in SLSC images, which will be exploited positively to increase, in turn, the brightness and detectability of small highly-coherent targets surrounded by tissues. Moreover, the target contrast will further improve in the presence of acoustic clutter, as SLSC is known to perform best in terms of image quality enhancement in such cases [19]–[22].

This paper investigates these concepts through a series of *in vitro* experiments, designed to investigate the three applications described above (i.e., microcalcification, kidney stone, and biopsy needle ultrasound imaging). The paper is organized as follows. Section II provides the theoretical background of the proposed idea, including a description of the methods implemented. Section III presents the experimental setup and the imaging scenarios considered. The obtained results are described in Section IV and discussed in Section V. Finally, Section VI summarizes our conclusions.

II. METHODS

A. Short-Lag Spatial Coherence Imaging

SLSC imaging provides images of the short-distance (i.e., lag) values of the backscattered echo spatial coherence and is based on the computation of the spatial covariance of signals across the receive aperture [11]. This aperture consists of N transducer elements, each receiving a radiofrequency (RF) echo signal, which is first delayed according to a given focal law. The delayed RF signals are referred to as $s_i(t)$, with i=1…N the index of the receiving element. The spatial covariance is computed as:

$$C(m) = \frac{1}{N-m} \sum_{i=1}^{N-m} \sum_{n=n_1}^{n_2} s_i(n) s_{i+m}(n) \tag{1}$$

where m is the lag between the RF signals, expressed in terms of number of transducer elements, and n denotes the n-th time/depth sample. [n_1 n_2] is a small kernel considered for covariance averaging, which is usually set equal to one wavelength. Spatial correlation R at lag m is then computed by normalizing the spatial covariance as follows:

$$R(m) = \frac{1}{N-m} \sum_{i=1}^{N-m} \frac{\sum_{n=n_1}^{n_2} s_i(n) s_{i+m}(n)}{\sqrt{\sum_{n=n_1}^{n_2} s_i^2(n) \sum_{n=n_1}^{n_2} s_{i+m}^2(n)}}. \tag{2}$$

Finally, the SLSC pixel (R_{SLSC}), represented in the resulting images, is obtained by integrating the spatial correlation over the first M lags:

$$R_{SLSC} = \sum_{m=1}^{M} R(m). \tag{3}$$

M is usually chosen by defining a certain percentage (Q) of the transmit aperture, i.e. M=N·Q/100. For example, in some initial papers on SLSC, it was suggested to set Q as the 1-30% of the transmit aperture [11].

B. Spatial Coherence in Multi-Line Transmit Imaging

MLT involves the transmission (TX) of multiple (N_{MLT}) simultaneous beams in the medium, in order to increase the frame-rate by a factor equal to the number of such beams [23]. This indeed changes the pulse-echo beam shape [18], [23], in that the received beam (h_{RX}) for the scan/focusing direction θ^{RX} has to be convolved with the full transmitted beam (h_{TX}), that includes N_{MLT} simultaneous beams focused along N_{MLT} directions θ_k^{TX}, with k=1…N_{MLT}:

$$h_{RX}(u) = \mathrm{sinc}\left(\frac{pu}{\lambda}\right) \mathrm{sinc}\left[\frac{Np}{\lambda}\left(u - \sum_{j=-\infty}^{+\infty} \frac{j\lambda}{p} - u^{RX}\right)\right] \tag{4}$$

$$h_{TX}(u) = \mathrm{sinc}(\frac{pu}{\lambda}) \sum_{k=1}^{N_{MLT}} \mathrm{sinc}[\frac{Np}{\lambda}(u - \sum_{j=-\infty}^{+\infty} \frac{j\lambda}{p} - u_k^{TX})]. \quad (5)$$

In (4) and (5), p is the N-element array pitch, λ is the wavelength, $u=sin(\theta)$ and θ is the steering angle; therefore, $u_k^{TX}=\sin(\theta_k^{TX})$ and $u^{RX}=\sin(\theta^{RX})$. The above equations clearly show that, by convolving h_{TX} and h_{RX}, some extra terms appear in the pulse-echo beam expression, which are the so-called crosstalk contributions caused by inter-beam interferences.

If we consider the system point spread function (PSF), crosstalk manifests as sidelobes surrounding the PSF main lobe in the axial direction (which is referred to as TX crosstalk), and as main-lobe replicas along the lateral direction (denoted as reception (RX) crosstalk) [23]. The presence of these secondary lobes increases with the number of simultaneously transmitted beams.

In our previous study [18], it was shown that MLT crosstalk alters the pulse-echo beam shape, which affects also the spatial coherence of backscattered echoes. Based on the van Cittert-Zernike theorem applied to pulse-echo ultrasound [24], in the standard Single-Line Transmission (SLT) case, the spatial coherence of diffuse scatterers measured at the focal depth is proportional to the Fourier transform of the squared transmit pressure field, i.e., to a triangular function, since (considering a uniform rectangular aperture) the squared one-way response is a $sinc^2$. However, in MLT, the beam shape changes, and spatial coherence of the diffuse scatterers drops towards zero in the short-lag region, particularly as the number of simultaneous TX beams increases [18] (see the Appendix). It was demonstrated that the spatial coherence has a triangular shape in the SLT case, as expected, while its trend has a damped-oscillation-like shape in the MLT case. The "strength" of such correlation loss is mainly linked to the number of transmitted beams, and thus to the increasing presence of crosstalk artifacts [18].

III. EXPERIMENTS

A. Ultrasound Acquisition Settings

All experimental acquisitions were carried out with the ULA-OP 256 research scanner [25], featuring 256 channels, connected to a 128-element phased array probe by Esaote (Esaote s.p.a., Florence, Italy), model PA230. The driving signal was a 2-cycle sinusoidal burst with Hanning tapering and a center working frequency of 2 MHz. Its amplitude was 64 V in SLT, while in MLT it was reduced by a factor equal to N_{MLT} (i.e. $64/N_{MLT}$ V). As MLT is implemented by superimposing the N_{MLT} excitation pulses that would be used to transmit each of the simultaneously transmitted beams, on some elements the signal amplitude could exceed the maximum allowed voltage on the specific used probe, i.e. 64 V in our case.

A custom mode for the ULA-OP 256 system was programmed to implement MLT with 2, 4, 6, 8, 12 or 16 simultaneous TX beams. We will refer to these configurations as 2-MLT, 4-MLT, 6-MLT, etc. Both for SLT and MLT modes, a Tukey apodization window with α=0.5 was applied in TX to reduce TX crosstalk, as proposed in [26]. 192 scan lines were acquired covering a 90° image sector and TX beams were focused at 40 mm depth. In RX, the analog gain was manually adjusted to exploit the 12-bit dynamic range of the analog-to-digital converters; the acquired RF signals were sampled at 19.5 MHz and sent to a computer via USB for processing in MATLAB (MathWorks, Natick, MA, USA).

In MATLAB, the received RF signals were first band-pass filtered to exclude unwanted noise outside the main working frequency band (1-3 MHz), and then dynamically focused and beamformed with DAS or SLSC. In the DAS case, after beamforming, the obtained RF images were envelope-detected through the Hilbert transform. The images were finally normalized and displayed on a logarithmic (dB) scale. In the SLSC case, two different Q values were considered to reconstruct the images, i.e. Q=30% and 50%, in order to explore the possible effect of different maximum lag values on the obtained image quality. Q values between 1-30% were suggested in previous work [11] [22]. We chose to use the upper bound of this range (Q=30%) and an even higher value (50%), as these values are expected to achieve better resolution [22] with acceptable contrast when visualizing the highly coherent targets of interest for the proposed work. The $[n_1\ n_2]$ temporal kernel was set equal to one wavelength. Finally, the absolute value of R_{SLSC} images was computed. Negative values were removed (to avoid biasing contrast measurements to incorrect values when reported on a dB scale), and resulting images were normalized and displayed on a logarithmic (dB) scale.

B. Imaging Targets

Tests were conducted in different imaging setups to emulate different types of small coherent targets in a background tissue, with or without an acoustic clutter source.

First, we tested the proposed idea on the wire targets embedded in the CIRS (CIRS Inc., Norfolk, VA) tissue-mimicking phantom model 040GSE. The probe was centered on the circular cross-section (diameter=100 μm) of four nylon wires, vertically spaced at increasing depths. This setup mimicked the scan of small bright targets (e.g., microcalcifications, despite the absence of clustering or different shapes).

Second, we used 3-mm diameter glass beads embedded in a lab-made phantom obtained from a mixture of 3.4% agar and 11.5% glycerin in water (Fig. 1a) [27]. This setup was employed to emulate kidney stones. In particular we acquired images of a bead placed at $(x, z)\approx(0, 31)$ mm.

Third, we considered the tip of a biopsy needle. A 18G biopsy needle was inserted into a piece of quite-uniform bovine meat (acquired through the standard food-supply commercial chain), first perpendicular (Fig. 1c) and then parallel to the probe, at approximately 30 mm depth.

In the three cases described above, acquisitions were repeated a second time by adding an acoustic clutter source, i.e. a metallic wire mesh [10], [28] (obtained by cutting 3 layers from a common kitchen scrubbing sponge), which was placed on the top surface of the phantom/meat, just under the probe (Figs. 1b and 1c). A thick (~1 cm) layer of ultrasound

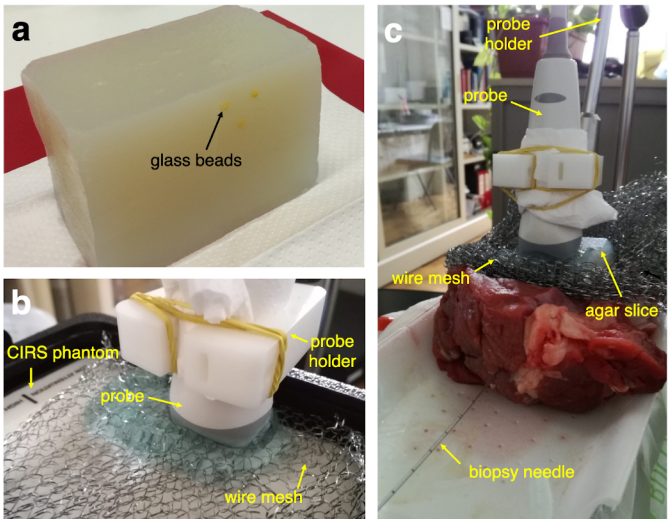

Fig. 1. Targets for image acquisitions: a) agar and glycerin phantom with glass beads (three beads are visible in the picture as small yellow spheres embedded in the phantom); b) top surface of the CIRS phantom, covered with the wire mesh and showing the PA230 probe; c) bovine meat sample with the wire mesh and with the biopsy needle inserted transversal to the probe.

gel was interposed between the metallic mesh and the probe, preventing their direct contact during acquisitions on the CIRS phantom (Fig. 1b). In the other two cases, a slice of the agar phantom (which is non-attenuating for ultrasound waves) was placed over the wire mesh plus gel as a separating layer (Fig. 1c), to facilitate probe positioning. The gel was also interposed inside the mesh to avoid the possible presence of air regions and create the required matching layer.

C. Evaluation Metrics

Considering our objective to enhance the detectability of small bright targets, we analyzed the contrast-ratio (CR) of such targets in the obtained images to quantify visibility:

$$CR = 20\log_{10}\left(\frac{\mu_{ROI}}{\mu_B}\right) \tag{6}$$

where μ_{ROI} is the mean value of a small region of interest (ROI) inside the target, centered around the brightest pixel, and μ_B is the mean value of a broader background region outside the target. The dimensions of these regions are reported in Table I for each test case. Mean values were computed considering envelope-detected DAS-beamformed signals and absolute values of SLSC-beamformed signals. In the latter case, negative values were removed from R_{SLSC} before computing its absolute value, in order to avoid biasing this measurement to incorrect values when reported on a dB scale [29].

We additionally measured the generalized contrast-to-noise ratio (GCNR) [30] (a newly proposed alternative to CNR and CR, able to resist to dynamic range alterations when different beamformers are compared), using these same image regions:

$$GCNR = 1 - \int \min\left\{p_{ROI}(\hat{y}), p_B(\hat{y})\right\} d\hat{y} \tag{7}$$

where p_{ROI} and p_B are the probability density functions of the signal amplitudes $\hat{y}$ inside and outside the target, respectively.

Texture Signal-to-noise ratio (T-SNR) was additionally evaluated, using the following equation:

$$T\text{-}SNR = \frac{\mu_B}{\sigma_B} \tag{8}$$

where σ_B is the standard deviation of values in the background region.

Finally, the different image formation techniques were compared in terms of lateral resolution (LR), using the CIRS phantom images. In particular, the wire located at $\theta \approx 0°$ and $z = \sim 36$ mm was used to evaluate LR by measuring its main lobe width at -6 dB. These coordinates refer to the case without the wire mesh placed on top of the phantom; for the case with clutter, the depth was increased by ~3 mm.

IV. RESULTS

Fig. 2 shows the trend of spatial coherence curves in all the considered targets, with and without clutter. The coherence relative to the background region is shown only for the agar phantom in which glass spheres were embedded (rightmost panels of Fig. 2) because those curves were similar in all test cases. Coherence trends were computed in the same regions used for CR, GCNR and T-SNR evaluation.

These results show that in SLT the coherence trend nearly approximates the expected curves when clutter is not added: for the wire target, the curves are relatively flat, given the small point-like target cross-section [11]; otherwise, the curves steadily decrease as lag increases. When MLT is applied, instead, coherence curves are partly lower than in SLT and show some oscillations. Only in the glass-bead case, curves are similar both in SLT and MLT. On the other hand, in the background (rightmost panel of Fig. 2) the loss of correlation caused by MLT is more significant, and curves quickly drop in the short-lag region when transmitting multiple beams, which is expected to contribute to a darker background in MLT SLSC images and thus an increased target contrast.

In addition, we also observe for the longitudinal needle case that the spatial coherence length is shorter than that of the other targets, which suggests that the use of lower Q values would be preferred for this case. To further demonstrate this difference, Fig. 2 highlights the position of lag 38 and 64 on the horizontal axis, which correspond to Q=30% and 50%, respectively.

TABLE I
SIZE OF IMAGE REGIONS USED FOR CR, T-SNR AND GCNR COMPUTATION

Test case	ROI (w×h)	Background (w×h)
Nylon wire in the CIRS phantom	0.7×0.7 mm^2	4×4 mm^2
Glass bead in the agar phantom	0.7×0.7 mm^2	14×14 mm^2
Biopsy needle in meat (transversal view)	0.7×0.7 mm^2	6×8 mm^2
Biopsy needle in meat (longitudinal view)	2.6×0.7 mm^2	15×6 mm^2

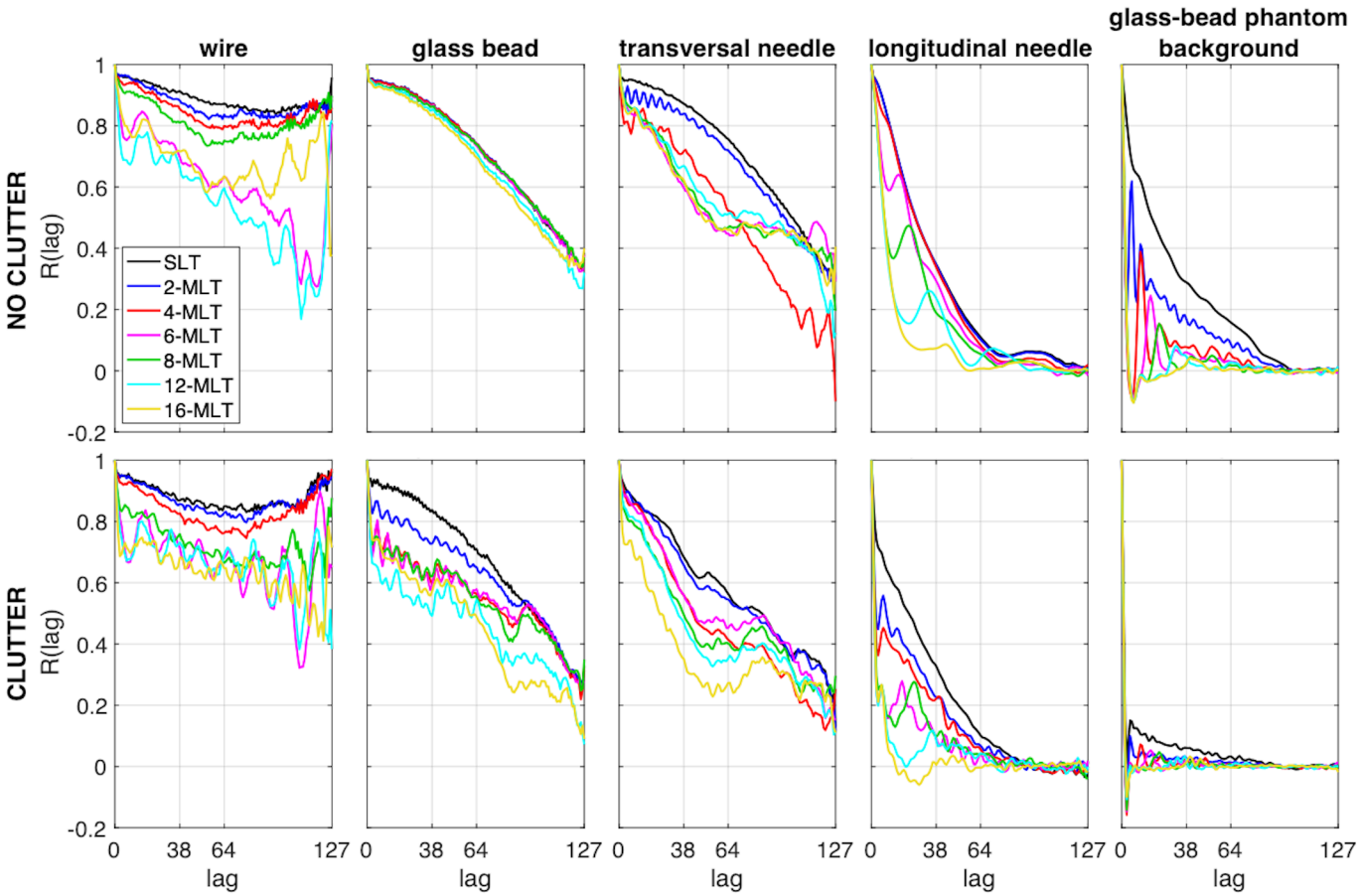

Fig. 2. Spatial coherence (R) as a function of lag, computed in the different imaging targets (from left to right: nylon wire, glass bead, transversal and longitudinal needle) and in the background of the agar phantom in which glass beads where embedded (rightmost panels of the figure). The top row refers to cases without clutter, while the bottom row to cases with clutter. The highlighted lags (38 and 64) correspond to Q=30% and 50%, respectively.

Finally, the presence of acoustic clutter degrades all curves, and it strongly affects the coherence measured in tissue background regions. The contrast enhancement provided by MLT SLSC is expected to be more pronounced in these cases.

Fig. 3 presents example images of the CIRS phantom, obtained with DAS and SLSC (Q=50%) beamforming, using SLT and 4/8/16-MLT, with the wire mesh generating acoustic clutter. For a more direct qualitative comparison, both SLSC and B-mode images were displayed on the same logarithmic scale with a 40-dB dynamic range. The measured performance parameters are shown in Fig. 4 for each analyzed configuration, with and without clutter. In these plots, GCNR values have not been reported, as they were almost always equal to 1, both for DAS and SLSC. This is because the small area inside the target included almost only very bright (white) pixels, and thus no overlap with the background region histogram occurred.

Qualitatively, Fig. 3 shows that DAS B-mode images are more affected by acoustic clutter than SLSC images. For DAS images, the background speckle looks brighter and more "filled up" as N_{MLT} increases, because of the presence of both clutter and (mainly RX) crosstalk artifacts. On the other hand, the background of SLSC images increases in darkness with increasing N_{MLT} values, and thus the nylon wires become more visible and brighter. These same trends can be observed also in the case without the wire mesh; however, the wire contrast with SLSC is lower, and consequently so is the improvement achieved with respect to DAS.

These observations are quantitatively confirmed with the top-left plot in Fig. 4, which shows that CR decreases by a few dBs over N_{MLT} with DAS, both with and without clutter. Alternatively, with SLSC, CR experiences large increases, generally up to 16-MLT. With SLSC, the CR becomes higher than that of DAS images above a N_{MLT} threshold that is lower than N_{MLT} =8 and N_{MLT}=4 without and with clutter present, respectively. The CR of SLSC images with the wire mesh (i.e., with clutter) is generally higher than that obtained without it. Another quantitative metric we considered is the maximum improvement of MLT SLSC when compared to SLT SLSC, as reported in Table II. For example, considering 16-MLT SLSC with Q=30% and clutter, CR increases by approximately 34 dB with respect to SLT SLSC.

The T-SNR values reported in the top-right panel of Fig. 4 also confirm that, as N_{MLT} increases, the background pattern in SLSC changes and a different behavior can be observed when compared to that of DAS images. With MLT SLSC, the mean background level decreases with N_{MLT}, as well as the standard deviation. The main effect observed is that background region becomes darker and partly also more uniform, with a consequent T-SNR decrease. On the contrary, DAS images show generally constant and higher T-SNR as N_{MLT} increases.

Regarding LR, the best values were generally obtained with

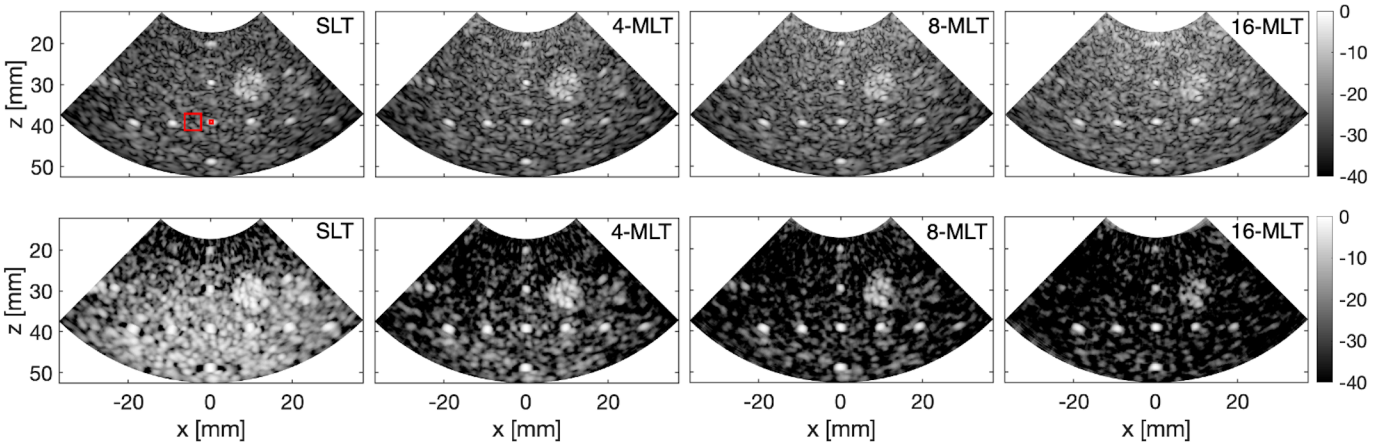

Fig. 3. Images of the nylon wires in the CIRS phantom, with acoustic clutter generated by the wire mesh, obtained with DAS (top row) and SLSC with Q=50% (bottom row). Columns correspond to different TX configurations, i.e. (from left to right) SLT, 4-MLT, 8-MLT and 16-MLT. Images are displayed with a 40-dB dynamic range. Red rectangles highlight the areas (ROI and background) used for CR, GCNR and T-SNR computation; the same wire was also used for LR evaluation.

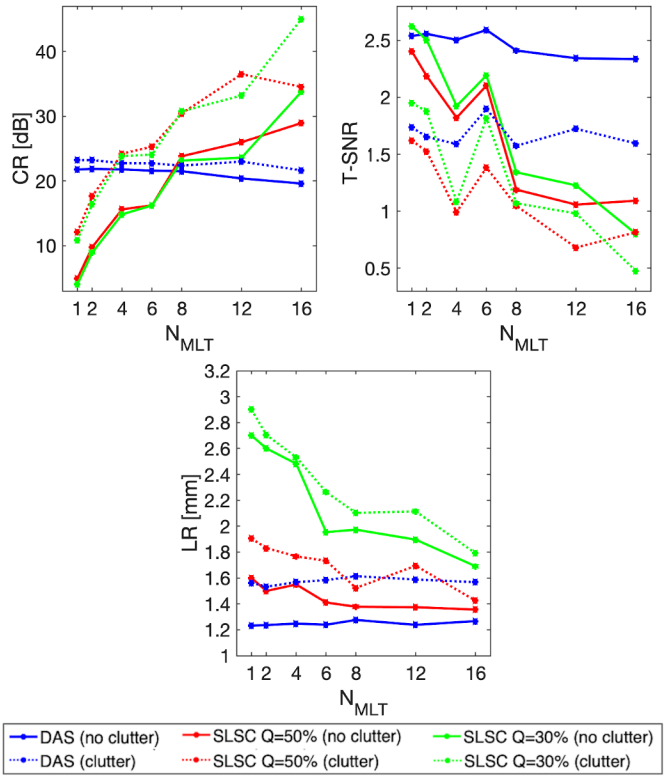

Fig. 4. CR (top left), T-SNR (top right) and LR (bottom) measured from images of the wires in the CIRS phantom, obtained with DAS, SLSC with Q=50% or 30%, and different numbers of simultaneous TX beams. The wire considered for measurements was the one at θ=0°, z=~39.1 mm in Fig. 3.

DAS images (see the bottom panel of Fig. 4). As expected, SLSC images created with Q=50% consistently perform better than those created with Q=30%. In addition, the LR of SLSC images generally improves with increasing N_{MLT}. For example, when clutter is present (dotted lines), LR with SLSC (Q=50%) is ~22% worse than with DAS in SLT, while for N_{MLT} =16 we have a ~9% improvement. On the other hand, MLT SLSC consistently allows better resolution performance compared to SLT SLSC, with maximum percentage improvements increasing from 15.3% to 38.2% with 16 simultaneous beams (Table II).

The results obtained in the second scenario, i.e. the 3-mm glass bead embedded in the agar phantom, are shown in Fig. 5, for DAS and SLSC with Q=30% and Q=50% in the presence of clutter. Fig. 6 presents the measured performance parameters in all configurations (with GCNR omitted for the same reasons described above).

Similarly to the previous test case, we observed increased CR with increasing N_{MLT} when SLSC was applied, and decreased CR with DAS applied instead. As the images in Fig. 5 show, with SLSC, the background is darker as N_{MLT} increases, and the small glass sphere gains higher contrast, while the opposite trend exists with DAS. Quantitatively, Fig. 6 shows that, when going from SLT to 16-MLT with clutter present, CR decreases by approximately 5 dB with DAS and increases by 15.9-17.3 dB with SLSC (Q=50% and 30%, cf. Table II). When no wire mesh was applied over the phantom instead, up to 25.6-26.5 dB improvement was achieved by SLSC with Q=50% and 30%, respectively, going from SLT to 16-MLT. Also, for MLT SLSC images, the T-SNR plots in Fig. 6 demonstrate a decrease as the number of simultaneous beams increases; differences with respect to DAS are more pronounced here than in the wire phantom images (right panel of Fig. 6).

Finally, the results for the biopsy needle in an *ex vivo* bovine meat sample are presented in Fig. 7, which shows the needle transversal view. The related quantitative trends are reported in Fig. 8. Images and plots for the needle longitudinal view are presented in Fig. 9 and Fig. 10, respectively. Similar to the above results, these cases are presented for images with added acoustic clutter, for SLT and 4/8/16-MLT.

As in previous cases (e.g., Figs. 3 and 5), Fig. 7 shows progressive darkening of the background in MLT SLSC images and consequent highlighting of the needle, which otherwise loses contrast in the DAS images, with increasing speckle brightness as N_{MLT} increases. We also observe a comet-tail artifact in Fig. 7 that is present just under the needle, which becomes less apparent when transmitting multiple beams.

Fig. 8 shows similar CR quantitative results to those

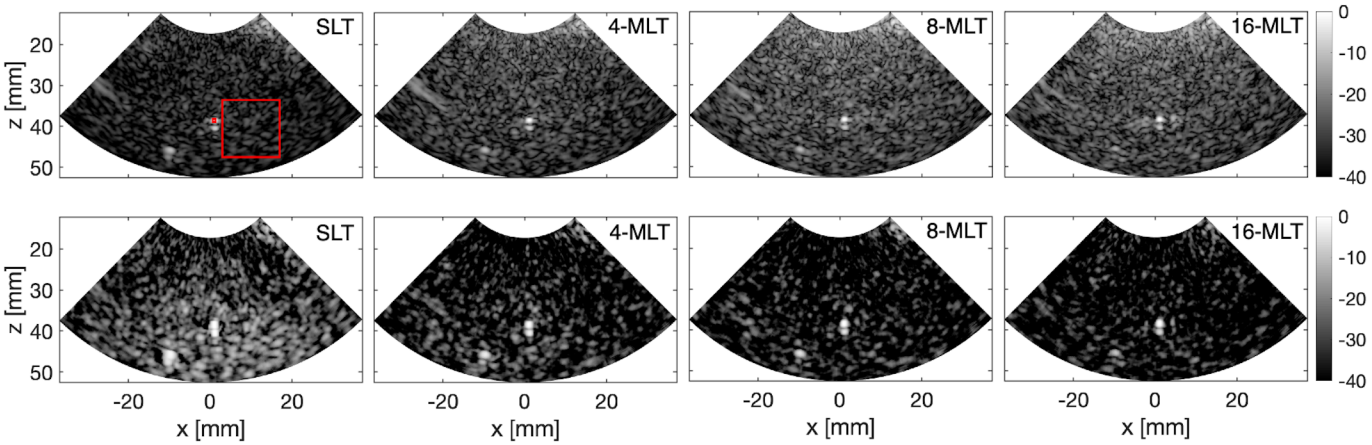

Fig. 5. Images of the 3-mm glass sphere in the agar phantom, with acoustic clutter generated by the wire mesh, obtained with DAS (top row) and SLSC with Q=50% (bottom row). Columns correspond to different TX configurations, i.e. (from left to right) SLT, 4-MLT, 8-MLT and 16-MLT. Images are displayed with a 40-dB dynamic range. Red rectangles highlight the areas (ROI and background) used for CR, GCNR and T-SNR computation.

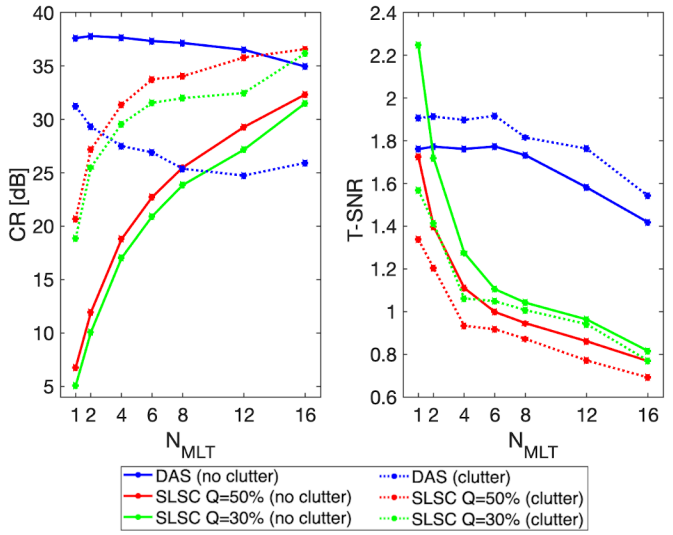

Fig. 6. CR (left) and T-SNR (right) for images of the glass sphere in the agar phantom, obtained with DAS, SLSC with Q=50% or 30%, and different numbers of simultaneous TX beams.

previously displayed. Specifically, the CR of DAS decreases as N_{MLT} increases, while in SLSC images CR increases with N_{MLT}. As shown in Table II, when no clutter is present, using SLSC with 16 simultaneous TX beams allows a maximum CR improvement of 32.7 dB and 28.7 dB as compared to SLT SLSC, when Q=30% and 50% are considered, respectively. This value becomes equal to about 6.5-6.7 dB in the case with acoustic clutter, applying 8- and 12-MLT, respectively.

For DAS images, T-SNR remains almost constant as N_{MLT} increases, while a decreasing trend is observed with SLSC images, for the same reasons previously explained.

For the needle longitudinal view, Fig. 9 shows similar results to Fig. 7, but here the resolution improvement of SLSC images with increasing numbers of simultaneous TX beams produces a more "dotted" appearance of the needle as N_{MLT} increases. In this particular case, the use of lower Q values seems to be more beneficial. For this reason, images are shown with both Q=50% and 30%.

In addition, both white and gray pixels appear within the target, thus GCNR results were also plotted in Fig. 10, as in this case they were not always equal to 1 (unlike the previous point-like targets).

The results in Fig. 10 show that SLSC images with different Q values have similar CRs. When clutter was not present (solid lines), the CR obtained with SLSC was generally lower than that of DAS B-mode images. With clutter present (dotted lines), SLSC offers the best results for all Q values and MLT configurations (N_{MLT}>1). For example, for SLSC with Q=30% (dotted green line), the highest CR (~28.8 dB) is achieved with N_{MLT}=2. With 12-MLT SLSC and Q=30%, CR decreases to about 21 dB.

In the no-clutter case (solid lines), the GCNR plots in Fig. 10 show that, for Q=30% and N_{MLT} > 4, SLSC offers the best results. In particular, the GCNR rises by up to 3.2% when using 6 simultaneous beams when compared to SLT DAS. For this same case, when Q=50%, GCNR is consistently worse than that of DAS, which agrees with the corresponding contrast results. However, when comparing MLT to SLT with SLSC, GNCR percentage improvements are as large as 80.4% when N_{MLT}=12 and Q=50%. When clutter is present (dotted lines in Fig. 10), GCNR no longer increases with increasing N_{MLT}, which is similar to the corresponding CR results. However, for SLSC images created with Q=30%, GCNR is generally better than that of the corresponding DAS results with clutter, except in the 16-MLT case (Fig. 10, green dotted lines in the panel on the right).

For this test case, the T-SNR of SLSC images experiences a significant decrease from SLT to 4-MLT, then remains generally constant for higher N_{MLT} values (Fig. 10, bottom panel). This observation is similar to that of CR and GCNR, which showed the largest variation when going from SLT to 4-MLT (although these parameters experienced an increase with N_{MLT}, rather than the decrease observed for T-SNR).

V. DISCUSSION

We demonstrated for the first time that the combined use of SLSC and MLT ultrasound imaging provides enhanced contrast and improved localization of small coherent targets in a tissue background. Our hypothesis relies on previous findings [18], showing that the presence of inter-beam

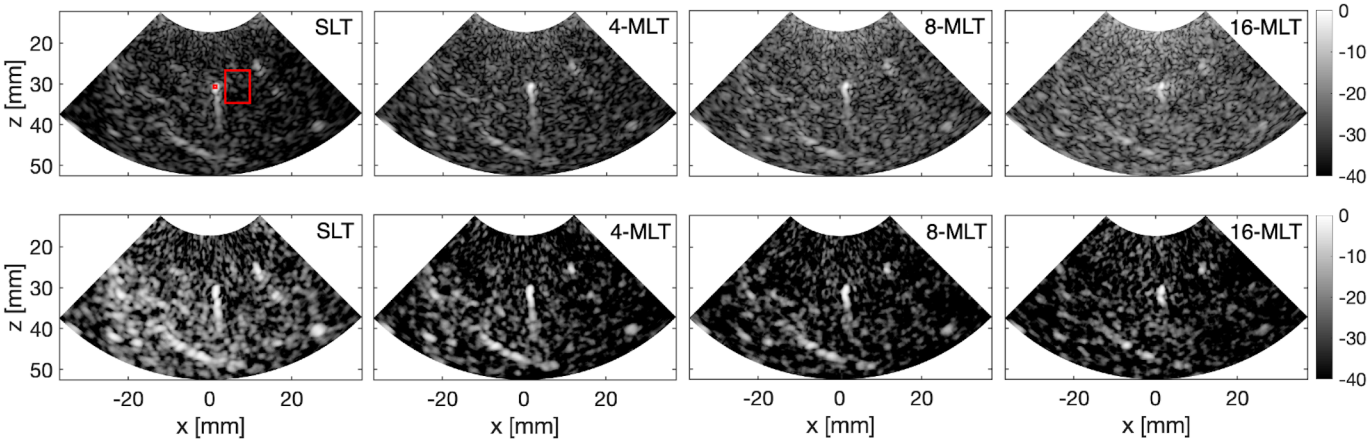

Fig. 7. Images of the biopsy needle inserted in the bovine meat sample transversally with respect to the probe, with acoustic clutter generated by the wire mesh, obtained with DAS (top row) and SLSC with Q=50% (bottom row). Columns correspond to different TX configurations, i.e. (from left to right) SLT, 4-MLT, 8-MLT and 16-MLT. Images are displayed with a 40-dB dynamic range. Red rectangles highlight the areas (ROI and background) used for CR, GCNR and T-SNR computation.

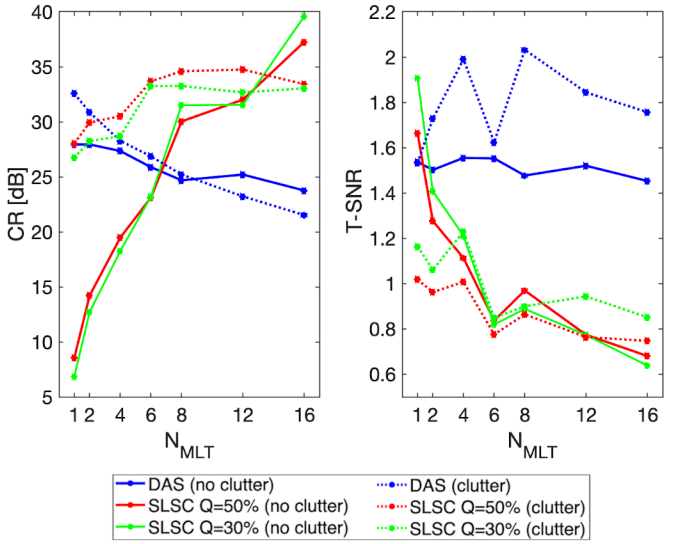

Fig. 8. CR (left) and T-SNR (right) for images of the biopsy needle inserted in the bovine meat sample transversally with respect to the probe, obtained with DAS, SLSC with Q=50% or 30%, and different numbers of simultaneous TX beams.

crosstalk contributions in the pulse-echo beam shape of MLT scans leads to a decrease of spatial coherence in the short-lag region (as reported in the Appendix). The novel contribution of this work combines MLT and SLSC to exploit this correlation loss and achieve MLT SLSC ultrasound images that improve the contrast of small reflective targets in the presence of acoustic clutter.

We considered three test scenarios with different target dimension, type and background medium, including a commercial tissue-mimicking phantom with nylon wires, a lab-made agar phantom with glass beads, and an *ex vivo* bovine meat sample in which a biopsy needle was inserted. For each scenario we tested our hypothesis also by adding an acoustic clutter source, i.e. 3 layers of a metallic wire mesh.

A phased array probe with 2 MHz center frequency was used, as done in previous works where we analyzed MLT jointly to other coherence-based algorithms [14], [18], [31]. Although frequencies higher than 2 MHz are typically employed (e.g., 3-5 MHz for kidney imaging, 7-13 MHz for breast), there is a known trade-off between frequency and depth penetration. The presence of challenging acoustic clutter is typically associated with the abdominal scans of large or obese patients, which often necessitates lower frequency ultrasound probes for appropriate penetration depth. In addition, our findings can be reasonably extended to probes with higher frequencies for other applications that can support shallower imaging.

In cases with a point-like targets, both with and without the addition of acoustic clutter, the GCNR was consistently near unity. However, SLSC CR increased with the number of simultaneous TX beams, showing a significant improvement between SLT and MLT configurations, e.g. with N_{MLT}>6, which is generally higher with high N_{MLT} than that of DAS images, particularly when clutter is present and Q is high. This is confirmed also by coherence trends measured within such targets and within the background regions, which further highlights that MLT generally causes a strong decrease of coherence in tissues, further supporting our initial hypothesis and the obtained CR estimates. The T-SNR values measured in background regions are generally lower with SLSC imaging, and they generally decrease further with MLT, which was not observed for DAS. This decrease is not due to an increased pixel variance, but to a reduction of both the mean and standard deviation of image values in the corresponding regions of interest. In particular, the main effect observed with MLT SLSC is a darkening of the tissue background (as noted throughout Section IV) and a partial uniformity increase, which represents an improvement of texture. In contrast to lesion detection applications, the observed texture uniformity improvement only partially contributes to the overall image quality improvement for the proposed task of detecting highly coherent targets, which is primarily achieved by the lower mean background level.

The correlation curves in Fig. 2 also highlight a difference that exists between the glass-bead and the other targets. In the former case, the curves are not particularly influenced by the number of TX beams in MLT. The reason may be that the

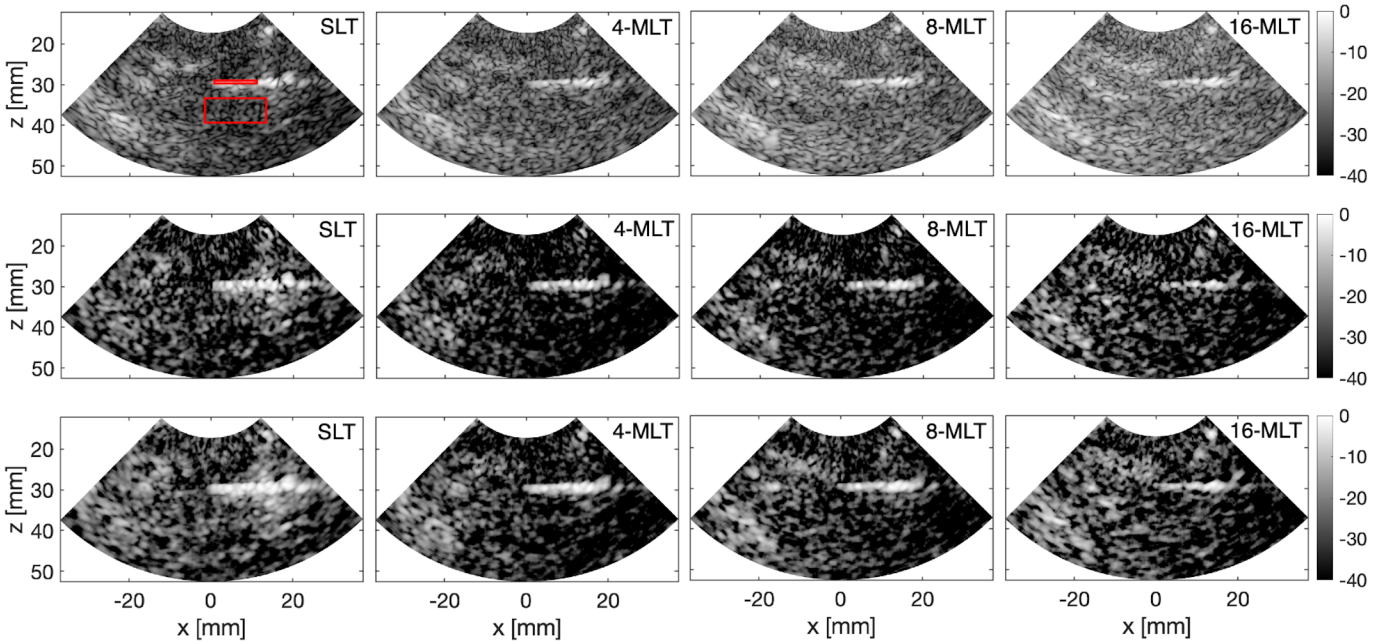

Fig. 9. Images of the biopsy needle inserted in the bovine meat sample longitudinally with respect to the probe, with acoustic clutter generated by the wire mesh, obtained with DAS (top row) and SLSC with Q=50% (middle row) or Q=30% (bottom row). Columns correspond to different TX configurations, i.e. (from left to right) SLT, 4-MLT, 8-MLT and 16-MLT. Images are displayed with a 40-dB dynamic range. Red rectangles highlight the areas (ROI and background) used for CR, GCNR and T-SNR computation.

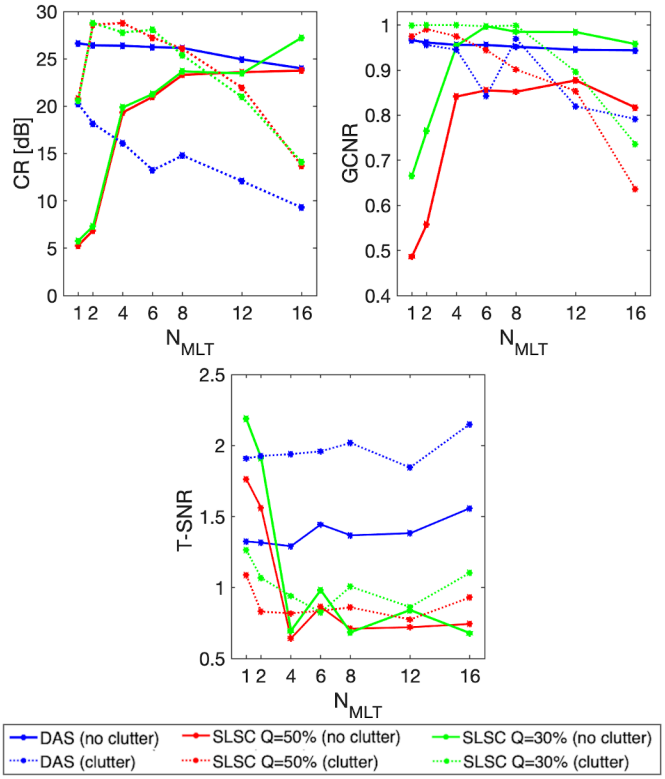

Fig. 10. CR (top left), GCNR (top right) and T-SNR (bottom) for images of the biopsy needle inserted in the bovine meat sample longitudinally with respect to the probe, obtained with DAS, SLSC with Q=50% or 30%, and different numbers of simultaneous TX beams.

reflectivity of the bead is significantly stronger than that of the agar background, as compared to the other analyzed cases (this could be seen by looking at the background of SLT images in in Fig. 5, which is darker than in Fig. 3 and Fig. 7). Thus, the agar background creates less artifacts that interfere with the coherence of the glass bead with MLT, and coherence curves within the target remain similarly high for all N_{MLT} values.

In images showing the longitudinal needle view, when no acoustic clutter was added, the CR trend was similar to that observed for point-like targets. However, in the presence of clutter, the CR trends are decreasing as N_{MLT} increases, both for DAS and SLSC (see Fig. 10). Although GCNR was equal to 1 in the majority of cases considered for point-like targets, in the needle longitudinal view images, instead, this parameter provided additional indications of possible improvements brought about by MLT SLSC as compared to DAS. Results show that, for this configuration, reducing Q in SLSC can be convenient (even if this implies reducing lateral resolution too), as it yields an improved GCNR and more uniform appearance of the needle shaft. However, even if the GCNR obtained with SLSC is higher than that of DAS, the improvement achieved with MLT (N_{MLT}>6) is limited.

Hence, together with the results obtained for CR and T-SNR, these results suggest that it could be beneficial to implement MLT to enhance the detectability of the needle in the longitudinal view (i.e., for large reflecting structures parallel to the transducer array) only for low N_{MLT} values, e.g. between 2 and 6. This last observation may likely be due to the needle shaft representing a longer target (~2.9-3 cm, i.e. about 38-39 wavelengths long, considering only the portion inserted in meat), thus more artifacts arise when multiple beams are transmitted, which are generated by each point in such structures. These artifacts create incoherent regions within the shaft itself, which limit the achievable CR improvement e.g. for N_{MLT}>6, even more when clutter is present. For this same reason, spatial coherence curves measured inside the needle shaft experience shorter coherence

TABLE II
MAXIMUM CR, GCNR, T-SNR AND LR VARIATION (AND ASSOCIATED FRAME-RATE INCREASE) WITH MLT SLSC COMPARED TO SLT SLSC

	Test case	MLT SLSC vs SLT SLSC			
		CR	GCNR	T-SNR	LR
NO CLUTTER (Q=30%)	Nylon wire	+29.7 dB (16×)	-	-69.4% (16×)	+37.4% (16×)
	Glass bead	+26.5 dB (16×)	-	-63.7% (16×)	-
	Needle (transversal)	+32.7 dB (16×)	-	-66.5% (16×)	-
	Needle (longitudinal)	+21.5 dB (16×)	+49.9% (6×)	-68.9% (16×)	-
CLUTTER (Q=30%)	Nylon wire	**+34.1 dB (16×)**	-	**-75.51% (16×)**	**+38.2% (16×)**
	Glass bead	+17.3 dB (16×)	-	-50.9% (16×)	-
	Needle (transversal)	+6.5 dB (8×)	-	-27% (6×)	-
	Needle (longitudinal)	+8.2 dB (2×)	+0.1% (4×)	-34.8% (6×)	-
NO CLUTTER (Q=50%)	Nylon wire	+24 dB (16×)	-	-56% (12×)	+15.3% (16×)
	Glass bead	+25.6 dB (16×)	-	-55.5% (16×)	-
	Needle (transversal)	+28.7 dB (16×)	-	-59.1% (16×)	-
	Needle (longitudinal)	+18.5 dB (16×)	**+80.4% (12×)**	-63.6% (4×)	-
CLUTTER (Q=50%)	Nylon wire	+24.4 dB (12×)	-	-57.9% (12×)	+25.2% (16×)
	Glass bead	+15.9 dB (16×)	-	-48.3% (16×)	-
	Needle (transversal)	+6.7 dB (12×)	-	-26.6% (16×)	-
	Needle (longitudinal)	+8 dB (4×)	+1.6% (2×)	-28.7% (12×)	-

Values in parentheses represent the frame-rate increase factor. Values in gray indicate a decrease. Values in bold highlight the greatest CR/GCNR/T-SNR/LR variation achieved.

lengths (see Fig. 2), and the curves drop near zero for lag values of ~76-78 (Q≈60%), then remain almost flat. This result provides further evidence supporting the choice of lower Q values in this kind of imaging experiment. In a possible future clinical setting, the Q value could be tuned in real-time by the operator depending on the specific application, as occurs with other parameters like time-gain-compensation or the focal depth.

While an LR improvement with MLT SLSC was noticed for increasing N_{MLT} values, LR was generally worse than that of DAS (Fig. 4). From this point of view, better results could probably be obtained by further increasing Q in SLSC images, at the expense of a greater computational complexity [22]. Nonetheless, given the clear identification of the needle tip in the SLSC images of Figs. 7 and 9, these LR differences are expected to have minimal impact on biopsy needle applications.

Measurements were mainly performed on targets placed at the focal depth, where spatial coherence is expected to be best when a classical scan with fixed TX focus and dynamic focusing in RX only is implemented [32], [33]. Generally, however, this effect is less prominent with higher TX F#s (e.g., F#>2). In particular, in our CIRS phantom images, the visibility of wires was reduced only at the shallower depths due to this effect. Nonetheless, our experiments were performed with a 2 MHz working frequency and a TX F# of about 2.5, considering Tukey apodization in TX and thus an effective aperture of 16 mm. The focal zone extended from 33 mm to 50 mm depth, when the -3 dB depth of field was measured from ultrasound field simulations (not shown), and from 27 mm to 65 mm depth when considering the -6 dB depth of field, with widths of 1.6 mm and 2.2 mm, respectively at the z=40 mm focus.

These focal zone measurements support our interpretation that coherence curves were primarily degraded by the presence of the wire mesh (and not by subtle differences of target placement in the absence and presence of the clutter-generating wire mesh, as the target was contained within the focal zone in each case). In addition, the correlation of the glass bead degraded in the presence of clutter, despite this target being closer to the 40 mm focal depth when compared to the no-clutter experiment (i.e., ~38.5 mm vs. ~31 mm depth, respectively).

The following three final remarks consider the impact of noise, the gray scale used for image display, and frame-rate on our proposed approach and assessment methods.

First, we know that in MLT the (temporal) signal-to-noise ratio of received signals decreases as N_{MLT} increases, due to the amplitude of the TX signal, which was reduced proportionally to N_{MLT} itself [14], [31]. We also know that SLSC performance improves as the presence of clutter and noise increases [11], [19], [22]. For this reason, we investigated whether the contrast improvement we observed was linked to the decrease of coherence in MLT, or rather to the lower signal-to-noise ratio obtained with such TX schema. We considered the amplitude of the 8-MLT excitation signal as a reference, and scaled the TX signal of SLT, 2/4/6-MLT by 8/4/2/1.5 times, respectively, so as to normalize all amplitudes to that of 8-MLT and achieve the same signal-to-noise ratio in all cases. We observed that the target contrast improvement still occurred with MLT SLSC, further validating our hypothesis.

Second, we showed both B-mode and SLSC images on a dB scale using a standard dynamic range (40 dB), despite SLSC images being displayed on a linear scale in many previous works [19], [21], [34]. We decided to display both image types on a dB scale for a more direct qualitative comparison with B-mode images. The value 40 dB was chosen because it corresponds to a range of [0.01; 1], which is close to the range that was used to display SLSC images on a linear scale in previous work. Choosing a linear display would improve the qualitative appearance of the SLSC images and choosing a higher dynamic range would worsen the qualitative display of the B-mode ultrasound images (as either more or less of the background region would be displayed with these adjustments and the contrast with the highly coherent targets

would be altered). Quantitative measurements comparing the performance of B-mode and SLSC were similarly implemented on the same scale (i.e., a linear scale) using envelope-detected, normalized signals for each image type.

We are aware that non-linear beamformers introduce potential issues due to the different dynamic range of beamformed signals when comparing the achieved image contrast. Therefore, we first considered the GCNR for contrast measurements, but in our particular case this metric did not reflect the actual differences of target visibility observed when visualizing images. An alternative is to use histogram matching [35]. However, considering the lack of a clear established reference for our intended objective (e.g., the reference could be SLT DAS, MLT DAS, or MLT SLSC), and given the discrepancies and inconsistences we observed when attempting to quantify performance based on histogram-matched images, we preferred not to employ this emerging technique to show images and perform subsequent quantitative analyses. Furthermore, the MLT SLSC images presented throughout this manuscript consist of small bright targets surrounded by a mostly dark background, which differs from more traditional histogram matching cases (i.e., speckle background with point- and cyst-like targets with different echogenicity, or cardiac images [14] [36]); thus, suitability toward our specific scenario deserves dedicated investigations that will be the focus of future work. The primary objective of the present work is to demonstrate that MLT either positively or negatively affects contrast when applied to SLSC or DAS images, respectively. Hence, we believe this effect of the associated physical properties must be analyzed on images as they are obtained immediately after these two fundamentally different image reconstruction processes are implemented, without further post-processing steps like histogram matching.

Third, in cases with limited contrast enhancement compared to SLT DAS, MLT SLSC possibly provides higher frame-rates too. Nevertheless, both SLSC and MLT involve higher computational costs/times and higher system requirements that could limit such frame-rate improvement; however, it should be considered that both techniques have been already implemented in real-time [34], [37]. Hence, employing MLT SLSC would be convenient, e.g. to keep a reasonable B-mode frame-rate in duplex or triplex modalities. It could also provide radiologists with a further indication of the target location, which is important during intraoperative imaging for an accurate real-time tracking of the tips of needles, catheters, or other tools, as well as of the target organs.

A similar result to that obtained by combining MLT and SLSC may be expected also when using other high-frame-rate techniques that employ unfocused waves (e.g. plane or diverging waves). In these cases, the image background representing tissue is expected to look darker when images are created with a single unfocused wave, likely at the expense of reduced resolution. While employing an increasing number of plane or diverging waves with coherent compounding will improve resolution, the coherence of background tissues is also expected to be improved, thus hindering the ability to provide the same benefits we demonstrated with MLT SLSC.

In a real clinical setting, the MLT SLSC technique could find application jointly to standard B-mode imaging in a bi-modal fashion: the latter would provide for an anatomical frame of reference, where the morphology of organs and tissues speckle are visible (e.g. for a proper navigation of needles), while the former would be overlaid on the B-mode map, providing a clearer and enhanced localization of highly-coherent targets in the investigated region.

VI. CONCLUSION

The presented results validate our initial hypothesis and show that combining SLSC and MLT enhances the detectability of small highly coherent structures in a tissue background, improving contrast. Possible applications which could benefit from this technique include breast microcalcification or kidney stone imaging. In addition, 2-D biopsy needle tracking, typically done in the longitudinal view, may partially benefit from the proposed technique, while 3-D biopsy needle tracking may benefit more significantly, due to the presented differences in needle appearance and CR with the transversal and longitudinal views. More specifically, MLT has the potential to increase volume rates, while MLT SLSC could potentially enhance needle detectability with 3-D imaging performed by scanning consecutive 2-D planes of the needle transversal view.

APPENDIX

In this section, further evidence of the spatial correlation trend obtained with MLT imaging is provided, both recalling simulation results obtained in [18] and adding new experimental measurements.

In [18], a 64-element phased array probe, with 340 μm pitch, working at 2 MHz was simulated. The TX focus was set at 70 mm depth, while dynamic focusing was applied in RX to scan a numerical uniform-tissue phantom; no apodization was applied in TX and RX in this case. The phantom size was $100\times1\times70$ mm^3, centered around (x, y, z) = (0, 0, 65) mm. SLT and MLT with 4/6/8/12 beams were implemented to scan a 90°-wide sector, and 192-line images were finally reconstructed with DAS. The normalized covariance [18] was then computed and averaged in a region centered at (x, z) = (0, 70) mm (TX focal depth), and the obtained plots as a function of lag are shown in Fig. 11A.

Similar trends to those observed with simulation results were experimentally demonstrated in the current manuscript, using the uniform agar-glycerin phantom and scan settings described in Section III. In this case, a small region included in a 2 mm axial range centered at the focal depth, and in the [-1.4°, +1.4°] angular range, was considered for the averaging of R values. Plots are reported in Fig. 11B for SLT and 2/4/6/8/12/16-MLT. Specifically, Fig. 11 shows that the trend of spatial coherence over lags rapidly decreases in the short-lag region and oscillates when MLT is employed. This means that the correlation among backscattered echo signals is high only for those signals received by very close elements in the active aperture, while it significantly decreases as soon as

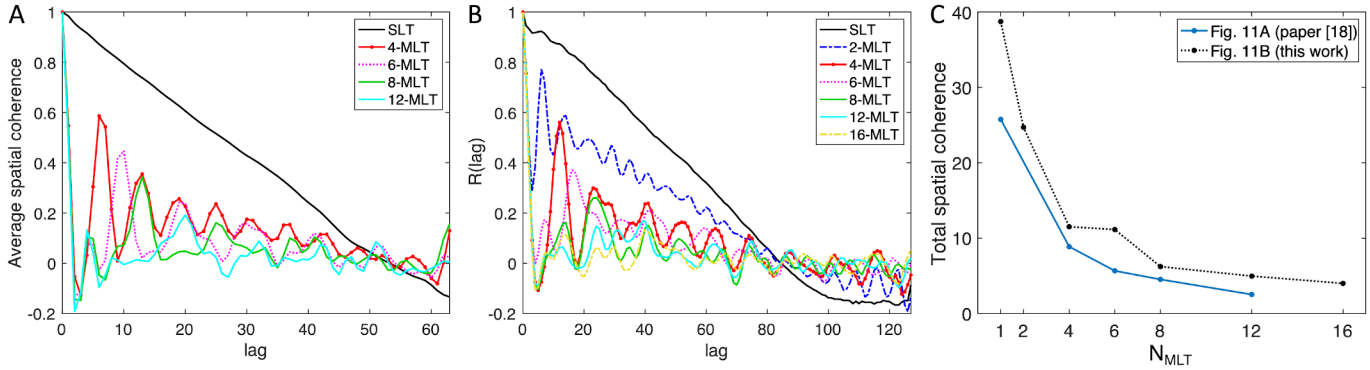

Fig. 11. Spatial coherence trend over lags for different SLT/MLT configurations: A) simulation results from [18], considering a 64-element aperture; B) experimental results from the present work, using a 128-element aperture; C) integral of the spatial coherence curves in A and B over all lags.

the elements are farther apart. For example, the curve for 12-MLT in Fig. 11B quickly decreases below 0, then oscillates, always remaining below ~0.17 for the higher lags. The advantage of this correlation loss is mainly linked to the number of simultaneous MLT beams, and thus to the increasing presence of crosstalk artifacts. To provide additional support for this observation, Fig. 11C shows that correlation globally decreases with N_{MLT}, when integrating the coherence curves over all lags.

These results provide the basis for the presented idea to combine MLT and SLSC: when MLT is employed, the coherence of backscattered tissues decreases; SLSC provides images of the spatial coherence itself, and thus, when implemented together with MLT, it is expected to generate images with a dark appearance of background tissues due to the observed correlation loss, which is increasingly evident as the number of simultaneously transmitted beams increases. This effect was exploited throughout this manuscript to increase the contrast of highly-reflecting targets. More specifically, as the background average grey level decreased, targets became more visible in the SLSC images, simultaneously gaining higher contrast and frame-rate with an increase in the number of simultaneously transmitted beams.

ACKNOWLEDGMENT

The authors thank Dr. P. Della Vigna (European Institute of Oncology, Milan, Italy) for the fruitful discussion on biopsy needle ultrasound imaging.

REFERENCES

[1] T. L. Szabo, *Diagnostic Ultrasound Imaging: Inside Out*. Elsevier, 2014. doi: 10.1016/C2011-0-07261-7.

[2] F. Stöblen *et al.*, "High-frequency Breast Ultrasound for the Detection of Microcalcifications and Associated Masses in BI-RADS 4a Patients," *Anticancer Res.*, vol. 31, no. 8, pp. 2575–2581, Jan. 2011.

[3] Y. L. Ouyang *et al.*, "A review of ultrasound detection methods for breast microcalcification," *Math. Biosci. Eng. MBE*, vol. 16, no. 4, pp. 1761–1785, 06 2019, doi: 10.3934/mbe.2019085.

[4] A. Wiacek *et al.*, "Robust Short-Lag Spatial Coherence Imaging of Breast Ultrasound Data: Initial Clinical Results," *IEEE Trans. Ultrason. Ferroelectr. Freq. Control*, vol. 66, no. 3, pp. 527–540, 2019, doi: 10.1109/TUFFC.2018.2883427.

[5] C. J. McCarthy, V. Baliyan, H. Kordbacheh, Z. Sajjad, D. Sahani, and A. Kambadakone, "Radiology of renal stone disease," *Int. J. Surg.*, vol. 36, pp. 638–646, Dec. 2016, doi: 10.1016/j.ijsu.2016.10.045.

[6] S. Ulusan, Z. Koc, and N. Tokmak, "Accuracy of sonography for detecting renal stone: Comparison with CT," *J. Clin. Ultrasound*, vol. 35, no. 5, pp. 256–261, 2007, doi: https://doi.org/10.1002/jcu.20347.

[7] V. Ganesan, S. De, D. Greene, F. C. M. Torricelli, and M. Monga, "Accuracy of ultrasonography for renal stone detection and size determination: is it good enough for management decisions?," *BJU Int.*, vol. 119, no. 3, pp. 464–469, 2017, doi: https://doi.org/10.1111/bju.13605.

[8] N. J. van de Berg, J. A. Sánchez-Margallo, A. P. van Dijke, T. Langø, and J. J. van den Dobbelsteen, "A Methodical Quantification of Needle Visibility and Echogenicity in Ultrasound Images," *Ultrasound Med. Biol.*, vol. 45, no. 4, pp. 998–1009, Apr. 2019, doi: 10.1016/j.ultrasmedbio.2018.10.004.

[9] T. L. de Jong, N. van de Berg, L. Tas, A. Moelker, J. Dankelman, and J. van den Dobbelsteen, "Needle placement errors: do we need steerable needles in interventional radiology?," *Med. Devices Evid. Res.*, vol. Volume 11, pp. 259–265, Aug. 2018, doi: 10.2147/MDER.S160444.

[10] M. A. L. Bell and J. Shubert, "Photoacoustic-based visual servoing of a needle tip," *Sci. Rep.*, vol. 8, no. 1, pp. 1–12, Oct. 2018, doi: 10.1038/s41598-018-33931-9.

[11] M. A. Lediju, G. E. Trahey, B. C. Byram, and J. J. Dahl, "Short-Lag Spatial Coherence of Backscattered Echoes: Imaging Characteristics," *IEEE Trans. Ultrason. Ferroelectr. Freq. Control*, vol. 58, no. 7, pp. 1377–1388, Jul. 2011, doi: 10.1109/TUFFC.2011.1957.

[12] J. Camacho, M. Parrilla, and C. Fritsch, "Phase coherence imaging," *IEEE Trans. Ultrason. Ferroelectr. Freq. Control*, vol. 56, no. 5, pp. 958–974, May 2009, doi: 10.1109/TUFFC.2009.1128.

[13] Pai-Chi Li and Meng-Lin Li, "Adaptive imaging using the generalized coherence factor," *IEEE Trans. Ultrason. Ferroelectr. Freq. Control*, vol. 50, no. 2, pp. 128–141, Feb. 2003, doi: 10.1109/TUFFC.2003.1182117.

[14] G. Matrone, A. Ramalli, J. D'hooge, P. Tortoli, and G. Magenes, "A Comparison of Coherence-Based Beamforming Techniques in High-Frame-Rate Ultrasound Imaging With Multi-Line Transmission," *IEEE Trans. Ultrason. Ferroelectr. Freq. Control*, vol. 67, no. 2, pp. 329–340, 2020, doi: 10.1109/TUFFC.2019.2945365.

[15] G. Matrone, A. S. Savoia, G. Caliano, and G. Magenes, "The Delay Multiply and Sum Beamforming Algorithm in Ultrasound B-Mode Medical Imaging," *IEEE Trans. Med. Imaging*, vol. 34, no. 4, pp. 940–949, Apr. 2015, doi: 10.1109/TMI.2014.2371235.

[16] J. E. Tierney *et al.*, "In vitro feasibility of next generation non-linear beamforming ultrasound methods to characterize and size kidney stones," *Urolithiasis*, vol. 47, no. 2, pp. 181–188, Apr. 2019, doi: 10.1007/s00240-018-1036-z.

[17] S.-W. Huang, J.-L. Robert, E. Radulescu, F. Vignon, and R. Erkamp, "Beamforming techniques for ultrasound microcalcification detection," in *2014 IEEE International Ultrasonics Symposium*, Sep. 2014, pp. 2193–2196. doi: 10.1109/ULTSYM.2014.0546.

[18] G. Matrone and A. Ramalli, "Spatial Coherence of Backscattered Signals in Multi-Line Transmit Ultrasound Imaging and Its Effect on Short-Lag Filtered-Delay Multiply and Sum Beamforming," *Appl. Sci.*, vol. 8, no. 4, Art. no. 4, Apr. 2018, doi: 10.3390/app8040486.

[19] J. J. Dahl, D. Hyun, M. Lediju, and G. E. Trahey, "Lesion detectability in diagnostic ultrasound with short-lag spatial coherence imaging," *Ultrason. Imaging*, vol. 33, no. 2, pp. 119–133, Apr. 2011, doi: 10.1177/016173461103300203.

[20] G. F. Pinton, J. Dahl, and G. Try, "Impact of clutter levels on spatial covariance: Implications for imaging," in *2010 IEEE International*

Ultrasonics Symposium, Oct. 2010, pp. 2171–2174. doi: 10.1109/ULTSYM.2010.5935460.

[21] M. A. Lediju Bell, R. Goswami, J. A. Kisslo, J. J. Dahl, and G. E. Trahey, "Short-Lag Spatial Coherence Imaging of Cardiac Ultrasound Data: Initial Clinical Results," *Ultrasound Med. Biol.*, vol. 39, no. 10, pp. 1861–1874, Oct. 2013, doi: 10.1016/j.ultrasmedbio.2013.03.029.

[22] M. A. Lediju Bell, J. J. Dahl, and G. E. Trahey, "Resolution and Brightness Characteristics of Short-Lag Spatial Coherence (SLSC) Images," *IEEE Trans. Ultrason. Ferroelectr. Freq. Control*, vol. 62, no. 7, pp. 1265–1276, Jul. 2015, doi: 10.1109/TUFFC.2014.006909.

[23] L. Tong, H. Gao, and J. D'hooge, "Multi-transmit beam forming for fast cardiac imaging--a simulation study," *IEEE Trans. Ultrason. Ferroelectr. Freq. Control*, vol. 60, no. 8, pp. 1719–1731, Aug. 2013, doi: 10.1109/TUFFC.2013.2753.

[24] R. Mallart and M. Fink, "The van Cittert–Zernike theorem in pulse echo measurements," *J. Acoust. Soc. Am.*, vol. 90, no. 5, pp. 2718–2727, Nov. 1991, doi: 10.1121/1.401867.

[25] E. Boni *et al.*, "ULA-OP 256: A 256-Channel Open Scanner for Development and Real-Time Implementation of New Ultrasound Methods," *IEEE Trans. Ultrason. Ferroelectr. Freq. Control*, vol. 63, no. 10, pp. 1488–1495, 2016, doi: 10.1109/TUFFC.2016.2566920.

[26] L. Tong, A. Ramalli, R. Jasaityte, P. Tortoli, and J. D'hooge, "Multi-Transmit Beam Forming for Fast Cardiac Imaging—Experimental Validation and In Vivo Application," *IEEE Trans. Med. Imaging*, vol. 33, no. 6, pp. 1205–1219, Jun. 2014, doi: 10.1109/TMI.2014.2302312.

[27] G. Matrone *et al.*, "An Experimental Protocol for Assessing the Performance of New Ultrasound Probes Based on CMUT Technology in Application to Brain Imaging," *JoVE J. Vis. Exp.*, no. 127, p. e55798, Sep. 2017, doi: 10.3791/55798.

[28] M. A. Lediju, M. J. Pihl, S. J. Hsu, J. J. Dahl, C. M. Gallippi, and G. E. Trahey, "A motion-based approach to abdominal clutter reduction," *IEEE Trans. Ultrason. Ferroelectr. Freq. Control*, vol. 56, no. 11, pp. 2437–2449, Nov. 2009, doi: 10.1109/TUFFc.2009.1331.

[29] A. A. Nair, T. D. Tran, and M. A. L. Bell, "Robust Short-Lag Spatial Coherence Imaging," *IEEE Trans. Ultrason. Ferroelectr. Freq. Control*, vol. 65, no. 3, pp. 366–377, Mar. 2018, doi: 10.1109/TUFFC.2017.2780084.

[30] A. Rodriguez-Molares *et al.*, "The Generalized Contrast-to-Noise Ratio: A Formal Definition for Lesion Detectability," *IEEE Trans. Ultrason. Ferroelectr. Freq. Control*, vol. 67, no. 4, pp. 745–759, Apr. 2020, doi: 10.1109/TUFFC.2019.2956855.

[31] G. Matrone, A. Ramalli, A. S. Savoia, P. Tortoli, and G. Magenes, "High Frame-Rate, High Resolution Ultrasound Imaging With Multi-Line Transmission and Filtered-Delay Multiply And Sum Beamforming," *IEEE Trans. Med. Imaging*, vol. 36, no. 2, pp. 478–486, 2017, doi: 10.1109/TMI.2016.2615069.

[32] N. Bottenus, B. C. Byram, J. J. Dahl, and G. E. Trahey, "Synthetic aperture focusing for short-lag spatial coherence imaging," *IEEE Trans. Ultrason. Ferroelectr. Freq. Control*, vol. 60, no. 9, pp. 1816–1826, Sep. 2013, doi: 10.1109/TUFFC.2013.2768.

[33] G. Matrone, A. S. Savoia, G. Caliano, and G. Magenes, "Depth-of-field enhancement in Filtered-Delay Multiply and Sum beamformed images using Synthetic Aperture Focusing," *Ultrasonics*, vol. 75, pp. 216–225, 2017, doi: 10.1016/j.ultras.2016.11.022.

[34] D. Hyun, A. L. C. Crowley, M. LeFevre, J. Cleve, J. Rosenberg, and J. J. Dahl, "Improved Visualization in Difficult-to-Image Stress Echocardiography Patients Using Real-Time Harmonic Spatial Coherence Imaging," *IEEE Trans. Ultrason. Ferroelectr. Freq. Control*, vol. 66, no. 3, pp. 433–441, Mar. 2019, doi: 10.1109/TUFFC.2018.2885777.

[35] N. Bottenus, B. C. Byram, and D. Hyun, "Histogram Matching for Visual Ultrasound Image Comparison," *IEEE Trans. Ultrason. Ferroelectr. Freq. Control*, vol. 68, no. 5, pp. 1487–1495, May 2021, doi: 10.1109/TUFFC.2020.3035965.

[36] A. Fatemi, S.-E. Måsøy, and A. Rodriguez-Molares, "Row–Column-Based Coherence Imaging Using a 2-D Array Transducer: A Row-Based Implementation," *IEEE Trans. Ultrason. Ferroelectr. Freq. Control*, vol. 67, no. 11, pp. 2303–2311, Nov. 2020, doi: 10.1109/TUFFC.2020.3001529.

[37] A. Ramalli *et al.*, "Real-Time High-Frame-Rate Cardiac B-Mode and Tissue Doppler Imaging Based on Multiline Transmission and Multiline Acquisition," *IEEE Trans. Ultrason. Ferroelectr. Freq. Control*, vol. 65, no. 11, pp. 2030–2041, Nov. 2018, doi: 10.1109/TUFFC.2018.2869473.